Highlights of Collaborated Research

Collaborative works with outside researches are carried out in consideration of the joint research program. Accepted applications are performed in following each division and facility of IMR.

1) Research Laboratories

Joint research conducted by out side researchers and IMR staff members at each research laboratory. Four categories “Research in Priority Areas”, “General Research”, “Exploratory Research for Young Researchers” and “Workshop” are prepared.

2) International Research Center for Nuclear Materials Science

This facility is open to university scientists all over Japan to support experiments using Japan Materials Testing Reactor, JMTR, the fast experimental reactor, JOYO, and the test reactor, JRR-3, operated by JAEA (Japan Atomic Energy Agency). The overseas reactor, BR2, located at the Belgian Nuclear Research Center, is also used for irradiation experiments. This facility acts as a hub for international collaborations; specimens irradiated in overseas reactors are accepted here for post-irradiation examinations by participating university researchers. Research subjects covered here include fundamental studies and R&D on fusion structural materials, high heat-flux materials, and a variety of functional materials, as well as engineering-oriented studies for the safety of light water reactors and basic researches supporting them. Materials studies utilizing radio-isotopes are also being conducted.

3) Advanced Research Center of Metallic Glasses (ARCMG)

ARCMG was established in April 2006, succeeding the Laboratory for Advanced Materials (LAM), investigating metallic glasses and other materials. This facility is open to domestic and international collaborations for research on all aspects of materials science, consisting of two major divisions: (i) scientific research on fundamental properties of materials, and (ii) development of engineering materials for practical usage. Micromotors, pressure sensors, fuel cell separators, soft magnetic material and many other devises using metallic glasses are proposed for practical applications.

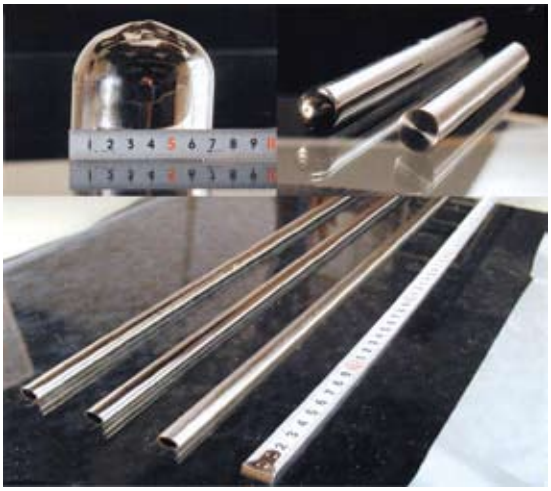

4) High Field Laboratory for Superconducting Materials

This laboratory restarted in 2001, succeeding “High Field Laboratory for Superconducting Materials” which was established in 1981. The main equipment is a hybrid magnet which generates steady high magnetic fields up to 31T. In addition, many cryogen-free superconducting magnets which have been developed by our laboratory are installed. Especially, we succeeded in developing the world’s first cryogen-free hybrid magnet, which generates 27.5 T. The laboratory also provides instruments for measuring various physical properties. These facilities are open to scientists and engineers on superconductors and other materials research.

5) Osaka Center for Industrial Materials research

The Osaka Center was established at Osaka as a special unit in IMR in April 2006 based on the agreement between Tohoku University and Osaka Prefecture Government. It is a laboratory dedicated to research and development of nano-structured metallic materials from the application viewpoints based on the basic research in the material science, chemistry and physics associated with research organizations in the Kansai region. Research in the Osaka Center is focused in particular on the understanding of the fundamental properties of nano-structured metallic materials and the rapid realization of their application to industry, in particular, the small and medium enterprises in Osaka area.

6) Center for Computational Materials Science

This center was developed from the Laboratory of Materials Information Science which was established in February 1989. Its main tasks are 1) administration and maintenance of the supercomputing system in this Institute, 2) maintenance of a supercomputing system network, 3) general support for the usage of the supercomputing system, 4) support of materials design by supercomputing simulation with vectorization and parallelization, 5) construction of factual database for materials in nonequilibrium phase , and 6) support of activity of Nanotechnology group on SINET3 and Asian Consortium for Materials Science, ACCMS-VO.

7) International Collaboration Center (ICC-IMR)

ICC-IMR was founded after the International Frontier Center for Advanced Materials in April 2008. It has evolved into the international research collaboration center of Institute for Materials Research. As such, ICC-IMR's programs have been expanded to include collaborative research projects by international teams. It works as a gateway of diverse collaboration between international researchers and IMR members. Currently, ICC-IMR coordinates five different programs: 1) International Integrated Project Research, 2) Visiting Professorships, 3) Short Single Research Visits, 4) International Workshops and 5) Coordination of International Collaboration. We welcome applicants from around the globe to participate in these international programs.

Formation of Nanotubes of Carbon by Joule Heating of Carbon-coated Si Nanochains

Carbon nanotubes (CNTs) are usually synthesized by chemical vapor deposition. We have found a new route to synthesizing CNTs. Insulating Si nanochains which are coated with hydrocarbon contamination are transformed into conducting CNTs by Joule heating. The transformation has been observed in situ on a TEM. The transformation can be utilized for selective formation of nanowire conducting paths.

Various types of nanostructure have been fabricated via template methods, in which template nanostructures are transformed into other types of nanostructure. In particular, the transformation of insulating nanostructures into conducting nanostructures has a great impact on nanodevice fabrications. We have found the transformation of insulating silicon nanochains into conducting nanotubes of carbon by Joule heating in a transmission electron microscope (TEM) [1, 2].

In a silicon nanochain, silicon nanoparticles are covered with and connected alternately by oxide to form a nanowire [3]. The Si nanochains were grown via an advanced vapor-liquid-solid (VLS) process using Au-Pb as a catalyst. Individual Si nanochains were heated by applying an electrical current using micro-manipulator system in a TEM to observe their structural change in situ. The Joule heating of a nanochain resulted in the transformation into a nanotube of carbon as shown in Fig. 1. Some Si nanoparticles were found in the nanotube. The current which was required for the transformation was typically as large as 10^1 nA with a bias voltage of 10^1 V.

It is very likely that the nanotube was formed from surface carbon contamination, followed by the evaporation of the core oxide. In fact, carbon was detected from the Si nanochains by means of Energy Dispersive X-ray spectrometry (EDX). When the Joule heating was insufficient, we found that the oxide core was only partly evaporated to make cavities. This evidences that the transformation occurs in two steps: first the surface graphene shell was formed, and then the core oxide evaporates. We estimated the temperature during the Joule heating. By considering the balance of Joule heating, thermal radiation, and thermal conduction to the electrodes, the temperature was estimated to be of the order of 10^3 K. This temperature is high enough for the evaporation of the oxide core.

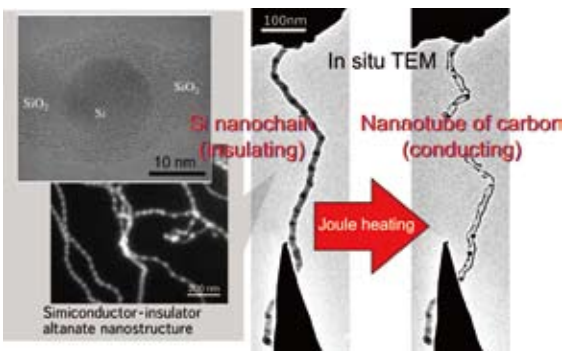

Fig. 1 Transformation of a carbon contaminated Si nanochain into a nanotube of carbon by Joule heating in a TEM.

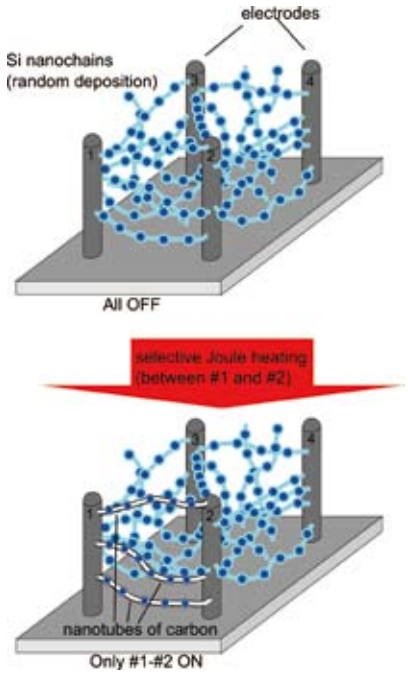

Fig. 2 Schematic illustration of the selective formation of conducting paths of nanotubes by Joule heating of Si nanochains.

Our finding enables us to change the charge transport properties of nanowires drastically, from insulating (nanochain) to conducting (nanotube): in a Si nanochain, the Si core is fragmented by insulating oxide, while carbon is a good conductor. We confirmed that the conductance of a formed nanotube was higher by an order of magnitude than a nanochain. Therefore, the transformation could be used for fabricating conduction paths (Fig. 2). When dispersing Si nanochains between predefined electrodes randomly with a sufficient density, all the paths are off. By applying a large bias voltage between a selected pair of electrodes, the path between the electrodes can be switched to the on state.

References

[1] T. Nogami, Y. Ohno, S. Ichikawa, and H. Kohno, Nanotechnology 20, 335602 (2009).

[2] H. Kohno, T. Nogami, S. Takeda, Y. Ohno, I. Yonenaga, and S. Ichikawa, accepted for publication in J. Nanosci. Nanotechnol.

[3] H. Kohno and S. Takeda, Appl. Phys. Lett. **73**, 3144 (1998).

Key Words

Si Nanochain, Carbon Nanotube, Joule Heating

Contact to

Hideo Kohno (Graduate School of Science, Osaka University)

E-mail: kohno@phys.sci.osaka-u.ac.jp

URL: http://tem.phys.sci.osaka-u.ac.jp/

Yutaka Ohno (Physics of Crystal Defects Division)

E-mail: yutakaohno@imr.tohoku.ac.jp

Room Temperature Layer-by-Layer Growth of InAlN Films on Lattice-matched ZnO Substrates

We have successfully grown $In_xAl_{1-x}N$ films on nearly lattice matched ZnO (000$\bar{1}$) substrates at room temperature (RT) by the use of pulsed laser deposition (PLD). We have found that reduction in growth temperature down to RT leads to suppression of the interfacial reactions between InAlN and ZnO and the layer-by-layer growth of InAlN.

$In_xAl_{1-x}N$ has attracted much attention because of the band gap ranging from 0.65 eV to 6.0 eV. However, it has been difficult to grow high quality InAlN films due to two major problems. The first problem is the phase-separation of InAlN that stems from the large miscibility gap between InN and AlN. The other problem is the lack of lattice-matched substrates. ZnO substrates have the same crystal structure and give the small lattice mismatch to InAlN. In spite of these advantages, ZnO has not been successfully used, since it easily reacts with nitrides at temperatures above 500 °C. The use of PLD low temperature growth technique enables us to solve the above-mentioned problems. In this study, we report on growth of high-quality InAlN films on ZnO substrates by the use of the RT growth technique [1].

Figures 1(a)-(c) show AFM images of InAlN films grown at 600 °C, 480 °C and RT, respectively. The film grown at 600 °C has quite a rough surface with a root mean square (RMS) value of 7.9 nm. In contrast, the surfaces of the films grown at 480 °C and RT were found to be smooth. Especially, the layer grown at RT clearly has a stepped and terraced surface, which is analogous to the morphology of the annealed ZnO surfaces. The RMS values for the surface roughness of the annealed ZnO and RT-InAlN terraces were 0.16 nm and 0.17 nm, respectively.

We performed XRD $2\theta/\omega$ measurements for InAlN layers grown at 600 °C, 480 °C and RT. The layer grown at 600 °C exhibits an extremely weak and broad peak, which indicates that the film quality is quite poor. The poor structural properties of films deposited at higher temperatures can possibly be attri buted to the rough interface between InAlN and ZnO, and the phase separation of InAlN. In contrast, a sharp InAlN 0002 peak appears when the growth temperature is reduced

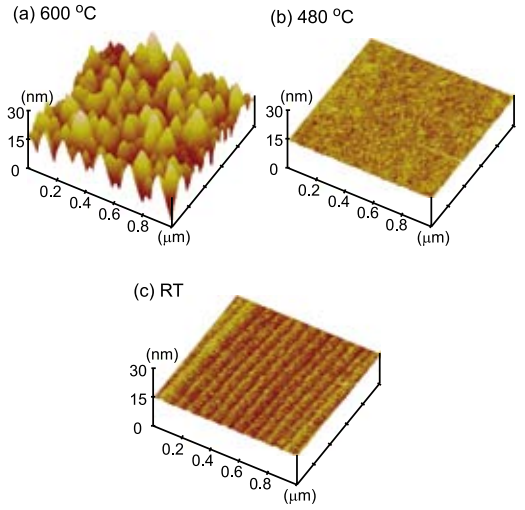

Fig. 1 AFM images of $In_{0.7}Al_{0.3}N$ films grown on ZnO substrates at (a) 600 °C, (b) 480 °C, and (c) RT by pulsed laser deposition. Atomically flat InAlN surface was obtained at RT.

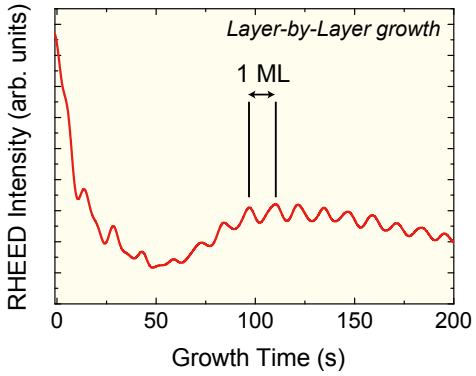

Fig. 2 Intensity profile of the specular spot in the RHEED pattern during room temperature growth of $In_{0.6}Al_{0.4}N$ on atomically flat ZnO surfaces. Clear RHEED oscillation indicates that the growth proceeded in the layer-by-layer mode from the initial stages.

to RT. Interpreting the peak position of this XRD data using Vegard's law showed that the In composition of the $In_xAl_{1-x}N$ layer grown at RT was $x = 0.7$

In order to evaluate the interfacial abruptness between $In_xAl_{1-x}N$ with a nominal In composition of $x = 0.7$ and ZnO, grazing X-ray reflectivity measurements were performed. It was found that the thickness of the interfacial layer between the InAlN layer and the ZnO substrate prepared at 600 and 480 °C was 2.7 nm and less than 1.0 nm, respectively. Although the interfacial layer of the sample grown at 480 °C is quite thin, the interface was so rough that damping of the X-ray reflectivity oscillation was observed, indicating that intermixing of InAlN and ZnO certainly took place. In contrast, the X-ray reflectivity oscillation of the sample prepared at RT is not seriously damped and the curve fits well with the two-layer model for an abrupt interface. This indicates that the interfacial reaction between the InAlN layer and the ZnO substrate has been drastically suppressed and an atomically abrupt InAlN/ZnO interface was obtained by reducing the growth temperature.

We also investigated the growth mode of InAlN on ZnO substrates at RT. Figure 2 shows the intensity profile of the RHEED specular spot during the growth of $In_{0.6}Al_{0.4}N$. We observed a clear RHEED oscillation, indicating that the growth proceeded in the layer-by-layer mode from the initial stages. Using the measured film thickness, one cycle of the oscillation was calculated to be 0.28 nm, which corresponds to ~1 monolayer of the *c*-plane.

References

[1] T. Kajima, A. Kobayashi, K. Shimomoto, K. Ueno, T. Fujii, J. Ohta, H. Fujioka, and M. Oshima, Appl. Phys. Express **3**, 021001 (2010).

Key Words

Group III Nitrides, Crystal Growth, Thin Films

Contact to

Hiroshi Fujioka (Institute of Industrial Science, The University of Tokyo)

E-mail: hfujioka@iis.u-tokyo.ac.jp

URL: http://fujioka.iis.u-tokyo.ac.jp

Laser-enhanced Chemical Vapor Deposition of Alumina for Cutting Tools

A laser-enhanced chemical vapor deposition (Laser CVD) is a new process to obtain ceramic coatings at extremely high deposition rates. Effects of deposition conditions on deposition rates, microstructures and crystalline phases of alumina coatings have been investigated in this study in order to apply this high-speed coating process to alumina coatings on cutting tools [1].

WC-Co composites are widely used as cutting tool materials, because they have high hardness and ductility at high temperature. In 1990s, alumina-coated WC-Co cutting tools were developed to elongate life-time of the cutting tools, and are generally used today.

In metalworking manufacturing industry, dry and high-speed lathe cutting process are required to improve productivity. However, dry and high-speed cutting process gives a severe high temperature and stressed environment to the cutting tools. Conventional alumina coatings usually contain alumina of γ- and κ-phase, and these phases are known to transform into the α-phase accompanying a volume change at a high temperature above 1000 K during the cutting process. Thus, alumina coatings in a single α-phase should be prepared on cutting tools for a dry and high-speed cutting process.

Although a conventional thermal CVD has been commonly applied for alumina coating on cutting tools, the deposition temperature of α-alumina coating is usually about 1300 K and such a high temperature degrades WC-Co substrate.

In this study, we prepared α-alumina films by LCVD and investigated the effect of deposition conditions on the deposition rates, microstructures and crystalline phases of alumina film. Aluminum tri-acetylacetonate ($Al(acac)_3$) was used as the precursor and was vaporized at vaporization temperature (T_{vap}) . Precursor vapor carried with argon gas and oxygen gas were separately introduced into the CVD chamber through a double-tube nozzle. The YSZ substrate was heated on a hot stage at pre-heating temperatures (T_{pre}) from room temperature to 973 K. An Nd:YAG laser was irradiated on the whole surface of the substrate.

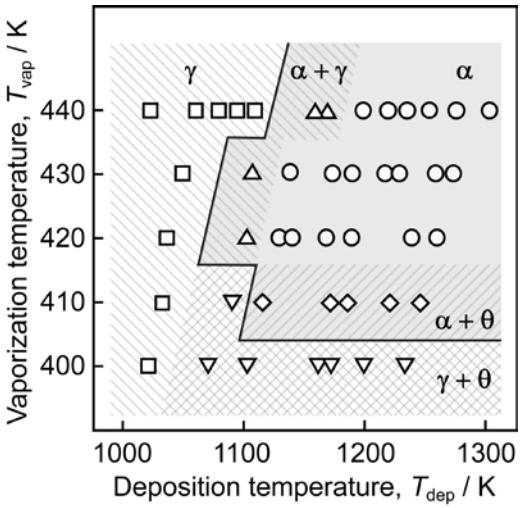

Fig. 1 Effect of deposition temperature(T_{dep}) and precursor temperature (T_{vap}) on the phase of alumina films.

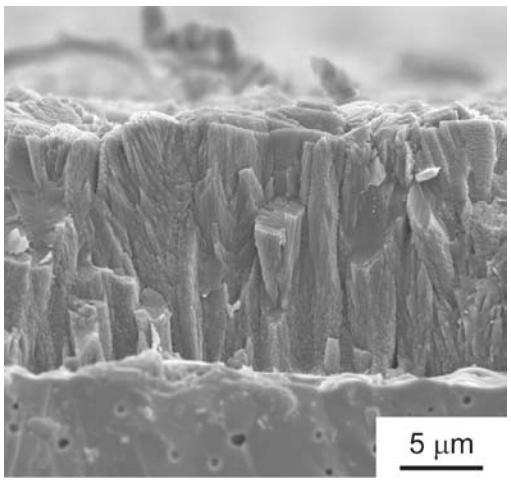

Fig. 2 Cross-sectional SEM image of α-alumina prepared at T_{vap} = 433 K.

Figure 1 depicts the effect of deposition temperature (T_{dep}) and precursor temperature (T_{vap}) on the phase of deposited alumina coating. At T_{dep} < 1060 K, α-alumina in a single phase were formed independently of T_{vap}. Alumina films with a α+θ mixture phase were formed at T_{vap} = 403 K and T_{dep} > 1070 K, whereas alumina films with a α+θ mixture phase were formed at T_{vap} = 413 K and T_{dep} > 1116 K. At T_{vap} > 423 K, the phase changed from a γ to a γ+α mixture to an α-phase with increasing T_{dep}.

The lowest temperature to obtain α-alumina was 1116 K in this study, which was about 200 K lower than that by thermal CVD.

A typical cross-sectional SEM image of α-alumina coating is shown in Fig. 2. The coating had a columnar structure and faceted surface.

References

[1] A. Ito, H. Kadokura, T. Kimura and T. Goto, J. Alloys and Compounds, **489,** 469 (2010).

Key Words

Laser CVD, Alumina Coating, Cutting Tool

Contact to

Teiichi Kimura (Japan Fine Ceramics Center)

E-mail: t_kimura@jfcc.or.jp

Takashi Goto (Multi-Functional Materials Science Division, IMR, Tohoku University)

E-mail: goto@imr.tohoku.ac.jp

Ferromagnetism and Superconductivity in UCoGe

Interplay of ferromagnetism and superconductivity has long been of great interest in solid state physics. Here we report microscopic coexistence of the two competing long-range ordered states as well as the presence of two nuclear-spin-lattice-relaxation rates in UCoGe [1].

It has been considered that internal magnetic inductions in a ferromagnet would suppress superconductivity and hence superconductivity could not coexist in a bulk ferromagnet. In some uranium-based ferromagnets that were recently discovered, however, it is expected that parallel-spin Cooper pairs (spin-triplet state) will form and survive even in a huge internal field. UCoGe is considered a promissing candidate for such an itinerant ferromagnet, characterized by a low Curie temperature T_C~2.5 K and a small ordered moment M_0~0.1μ_B/U [2]. Superconductivity with T_{SC}~0.5 K was confirmed in bulk measurements, but it was unclear whether the superconductivity microscopically coexists with the ferromagnetism.

We installed a tetra-arc furnace at Laboratory of α-Ray Emitters, IMR to prepare a single crystalline material of good quality including uranium element. Figure 1 shows a snap shot of the single crystal growth. The obtained single crystals exhibited a jump in the specific heat at T_{SC}, indicating a bulk phase transition. Then, we carried out ^{59}Co NQR (nuclear quadrupole resonance) experiments [1]. NQR signals below 1 K indicated ferromagnetism throughout the sample volume. We also studied the nuclear spin-lattice relaxation rate $1/T_1$. As shown in Fig. 2, the rate decreases rapidly below T_{SC}, roughly T^3, suggestive of line nodes in a superconducting gap. This provides unambiguous evidence for the microscopic coexistence of ferromanetism and superconductivity.

One may notice that in addition to the slow component as mentioned above, a fast component at the ferromagnetic signal emerges in the superconducting state. The latter is roughly proportinal to temperature, consistent with Korringa behavior characteristic of metals. This indicates that it originates from non-superconducting regions. One possibility of this intriguing feature is a nonunitary superconducting state, as in superfluid ^{3}He. Another possibility is a self-induced vortex state, which has never been identified experimentally. These results shed a new light on the "classical" issue of the interplay between ferromagnetism and superconductivity.

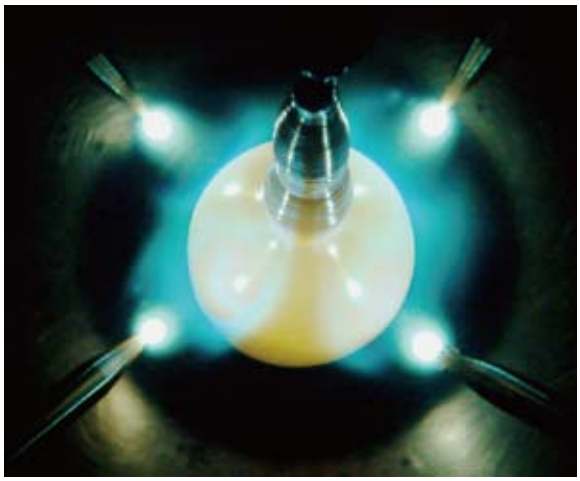

Fig. 1 Picture of single crystal growth using a tetra-arc furnace installed at IMR.

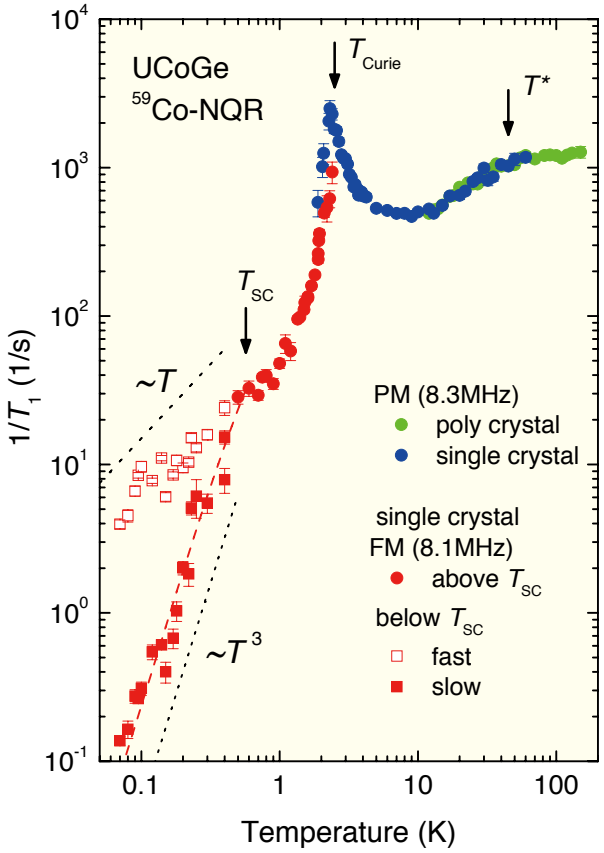

Fig. 2 Temperature dependences of ^{59}Co relaxation rate in the single crystalline sample, along with the rate in the poly crystal between 10 and 150 K [1].

References

[1] T. Ohta, T. Hattori, K. Ishida, Y. Nakai, E. Osaki, K. Deguchi, N. K. Sato and I. Satoh. J. Phys. Soc. Jpn. **79**, 023707 (2010).

[2] N. T. Huy, A. Gasparini, D. E. de Nijs, Y. Huang, J. C. P. Klaasse, T. Gortenmulder, A. de Visser, A. Hamann, T. Gorlach, and H. v. Lohneysen, Phys. Rev. Lett. **99**, 067006 (2007).

Key Words

UCoGe, Ferromagnetic Superconductor, Heavy Fermion

Contact to

Noriaki Sato (Department of Physics, Nagoya University)
E-mail: kensho@cc.nagoya-u.ac.jp
Kenji Ishida (Department of Physics, Kyoto University)
E-mail: kishida@scphys.kyoto-u.ac.jp

Microstructures and Reaction Mechanism of Aluminum Hydride

A promising hydrogen storage material, AlH_3 was investigated by transmission electron microscopy (TEM) and associated electron energy-loss spectroscopy (EELS). Microstructural and electronic structural changes associated with hydrogen desorption were in situ observed for the first time. In addition, EELS of AlH_3 and its derivative phases revealed the electronic structure changes during the hydrogen desorption process. The hydrogen desorption mechanism is discussed based on the observation and theoretical calculations.

Aluminum trihydride (AlH_3, alane) is considered as one of the promising advanced hydrogen storage materials because of its high gravimetric and volumetric hydrogen densities, relatively low hydrogen desorption temperature and stability at an ambient environment [1]. It is important to investigate the microstructural and electronic structural changes during the hydrogen desorption process, which could be a clue to understand the reaction mechanism of this material. It was, however, extremely difficult to observe alane particles in TEM because high energy electron illumination instantly starts to decompose the material into metallic aluminum. We successfully observed the hydrogen desorption process *in situ* with TEM for the first time by reducing the accelerating voltage down to 100 kV and minimizing the electron dose, using a high sensitivity CCD camera. At the same time, we also recorded electron energy-loss spectra (EELS) of alane and its derivative phases, which convey the chemical bonding information of those phases [2].

Figures 1(a)-(c) show *in situ* TEM observation of hydrogen desorption process by high energy electron irradiation at RT, and the corresponding low loss EELS spectra are shown in (d) [2,3]. The TEM images clearly show that the hydrogen desorption process ($AlH_3 \rightarrow Al + 3/2H_2$) proceeds by a nucleation-and-growth mechanism of metallic Al particles. AlH_3 and metallic Al exhibit their intrinsic plasmon peaks at 16.7 and 15.1 eV, respectively, due to their different band structures and valence electron densities [2], as shown in Fig. 1(d). At the intermediate state of decomposition (Fig. 1(b)), the two plasmon peaks coexist (spectrum #2 in (d)), indicating that this process is a first order phase transition. Furthermore, it was found that a single crystalline alane particle is covered by a thin amorphous layer, which shows no external shape change before and after the desorption reaction. This suggests that the layer stabilizes the AlH_3 and

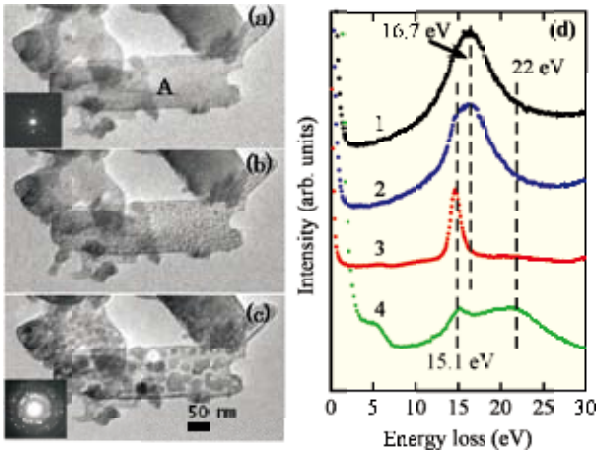

Fig. 1 (a)-(c) In situ TEM observation of hydrogen desorption reaction $AlH_3 \rightarrow Al + 3/2H_2$ and corresponding electron diffraction. (d) Low loss spectra 1-3 correspond to TEM images (a)-(c), respectively. Spectrum 4 is acquired near the surface layer of the decomposed particle A in (c).

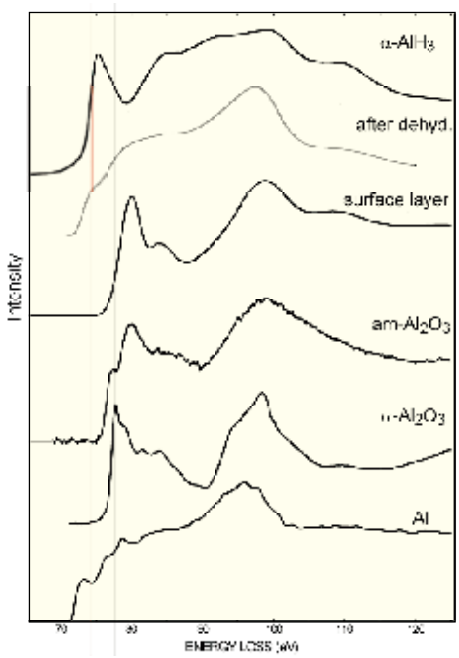

Fig. 2 Al $L_{2,3}$ core-loss EELS (2p → 3d* transition) from the indicated phases and reference spectra from the known materials to identify each observed phase.

prevents the particle from the hydrogen desorption reaction at ambient temperature and pressure. Once a part of alane particle is decomposed, the hydrogen molecules perforate the alumina (Al_2O_3) layer by the increasing internal pressure, which catastrophically triggers the entire decomposition.

Al $L_{2,3}$ core-loss EELS (2p → 3d* transition) from the indicated phases and reference spectra from the known materials are shown in Fig. 2. The top spectrum from alane was restored from the low signal-to-noise ratio experimental spectra, using the PIXON method [4] because of spectrum acquisition at the very low electron dose. The spectral profile was reproduced by a theoretical prediction based on the α-AlH_3 structure [2], which confirmed that alane is a covalent bonding material and weak covalent bonding between the second neighboring Al-Al pairs.

The low loss EELS from the surface layer is also shown as #4 in Fig. 1(d). The surface protecting layer is thus identified from the low-loss and core-loss EELS to be amorphous alumina (Al_2O_3), comparing the spectrum with the reference ones.

References

[1] S. Orimo, Y. Nakamori, T. Kato, C Brown and C. M. Jemsen, Appl. Phys A **83**, 5 (2006).
[2] S. Muto, K. Tatsumi, K. Ikeda and S. Orimo, J. Appl. Phys. **105**, 123514 (2009).
[3] Kinken Research Highlights 2009, p.22.
[4] S. Muto, R. C. Puetter and K. Tatsumi, J. Electron Microsc. **55**, 215 (2006).

Key Words

Aluminum Hydride, Transmission Electron Microscope, Electron Energy-loss Spectroscopy

Contact to

Shunsuke Muto (Graduate School of Engineering, Nagoya University)
E-mail: s-mutoh@nucl.nagoya-u.ac.jp

Highly-arranged Nanoscale Phase Separation in Epitaxially-Grown III-V Semiconductor Alloys

We prepared TlInGaAsN/TlInP quantum well structures using gas source molecular beam epitaxy and characterized them by means of transmission electron microscopy and scanning transmission electron microscopy. It was found that naturally-formed vertical quantum wells with a periodicity of ~1 nm are formed in TlInGaAsN layers.

The introduction of structurally and/or compositionally modulated structures into semiconductor materials is of technological importance for adding desirable functionalities to electronic and optoelectronic devices. Spontaneous formation of nanostructures during crystal growth, the so-called self-assembly or self-organization, is one of the useful ways to introduce the modulated structure to materials in atomic scale. Here we demonstrate that nanoscale phase separation perpendicular to the growth direction can be realized in III-V semiconductor alloys [1,2].

TlGaInAsN/TlInP multiple quantum well structures were grown at 420 °C on InP(100) substrates by gas source molecular-beam epitaxy. Figure 1(a) shows a cross-sectional bright-field TEM image of the obtained specimen, viewed along the [110] direction. The TlGaInAsN (bright contrast) and TlInP (dark contrast) layers are alternatively stacked. The TlInP layers reveal uniform diffraction contrast, whereas a modulated structure exists in the TlGaInAsN layers. In the electron diffraction pattern (inset), satellite reflections are apparent on both sides of the Bragg reflections, indicating that the modulated structure is highly arranged. The modulation period was estimated to be ~1 nm. On the other hand, no modulation was observed in the image and diffraction pattern viewed along the [1$\bar{1}$0] direction. That is, vertical quantum wells are formed in the TlGaInAsN layers. From the HAADF-STEM (Fig. 1(b)) and EDX analyses, it was found that the modulated structure consists of Ga- and In-rich regions, indicating that nanoscale phase separation occurs along the lateral direction.

We discuss the formation process of nanoscale phase separation based on a simple kinetic Ising model in which the rearrangement of atoms occurs at the topmost layer only and the atomic configuration is frozen-in when the surface is covered with a next monolayer [3,4]. In this model, pairwise atomic interactions up to the second nearest neighbors are

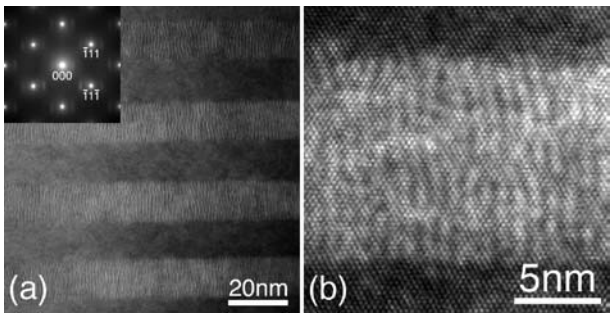

Fig. 1 (a) Bright-field image and electron diffraction pattern of TlGaInAsN/TlInP multiple quantum well structure. (b) HAADF-STEM image of TlGaInAsN layer.

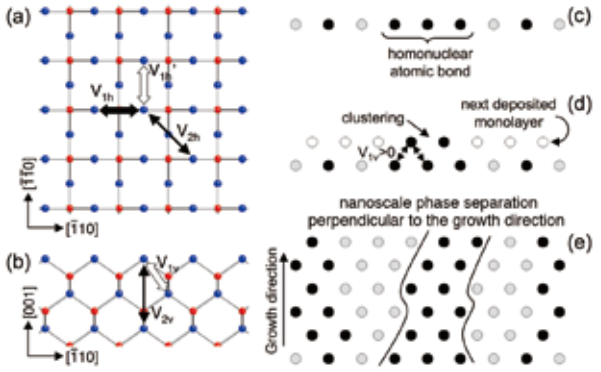

Fig. 2 (a,b) Pairwise atomic interactions at the topmost layer of an $(A_{1-x}B_x)_{0.5}C_{0.5}$ alloy. (a) Plan-view and (b) cross-sectional view. A and B (blue) are group-III elements and C (red) is a group-V element, or *vise versa*. (c-e) Formation process of like-atom chains along the growth direction. Only group-III elements are drawn, and black and gray circles correspond to A and B atoms, respectively.

considered (Figs. 2(a) and 2(b)). From Monte Carlo simulations, it was found that the pairwise atomic interactions are defined as follows: $V_{1h}<0$, $V_{1h}'>0$, $V_{2h}<0$, $V_{1v}>0$, and $V_{2v}<0$, where the positive and negative values prefer homonuclear (Ga-Ga and In-In) and heteronuclear (Ga-In) atomic pairs, respectively. When the growth temperature is low and the migration of atoms is suppressed, the ordering on the surface proceeds incompletely and homonuclear bonds are inevitably formed (Fig. 2(c)). Once such homonuclear bonds are formed, the same atoms preferentially assemble on them in the next deposited monolayer due to the positive interaction V_{1v} (Fig. 2(d)). The epilayer thus obtained includes like-atom clusters which elongate along the growth direction (Fig. 2(e)).

References

[1] M. Ishimaru, Y. Tanaka, S. Hasegawa, H. Asahi, K. Sato and T. J. Konno, Appl. Phys. Lett. **94**, 153103 (2009).

[2] M. Ishimaru, Y. Tanaka, S. Hasegawa, H. Asahi, K. Sato and T. J. Konno, Proc. 21st Int'l Conf. Indium Phosphide and Related Materials, 253 (2009).

[3] M. Ishimaru, S. Matsumura, N. Kuwano and K. Oki, Phys. Rev. B **51**, 9707 (1995): **52**, 5154 (1995): **54**, 10814 (1996).

[4] M. Ishimaru, S. Matsumura, N. Kuwano and K. Oki, J. Appl. Phys. **77**, 2370 (1995).

Key Words

Self-assembly, Phase Separation, Ordering

Contact to

Manabu Ishimaru (Institute of Scientific and Industrial Research, Osaka University)

E-mail: ishimaru@sanken.osaka-u.ac.jp

Toyohiko J. Konno (Advanced Analysis of Materials Division, IMR, Tohoku University)

E-mail: tjkonno@imr.tohoku.ac.jp

Si-based Light-emitting Devices Based on Ge Quantum Dots in Optical Microcavities

Ge self-assembled quantum dots were embedded into Si microcavities as active centers. Resonant luminescence was observed at telecommunication wavelengths at room-temperature. The results show a promising method for Si-based light source for optoelectronic integration on Si platform.

Optoelectronic hybrid integration on Si platform is one of the solutions for the next-generation integrated circuits. Therefore, Si-based light-emitting devices are inevitable for the hybrid integration. Various proposals have been reported for Si-based light-emitting devices in recent years. Among them, Ge self-assembled quantum dots are one possible candidate of Si-based light-emitting devices. The advantages of Ge self-assembled dots are the full compatibility to CMOS technology and the light emission at the telecommunication wavelengths. Unfortunately, light emission from Ge dots is still lack of efficiency and spectrum purity, especially at room temperature. In order to enhance the light emission, Ge dots were embedded into various optical microcavities, such as photonic crystal microcavities and microdisk resonators. Photoluminescence (PL) measurement results show strong resonant light emission from Ge quantum dots in these microcavities at room-temperature (RT) [1, 2].

Figure 1 shows the schematic structure of the device. The devices were fabricated using standard fabrication techniques. First, three layers of the quantum dots were grown on Si-on-insulator (SOI) wafers in Stranski-Krastanov mode using gas-source molecular-beam epitaxy at 600°C. Electron-beam lithography, reactive-ion etching, and wet etching were used to pattern optical microcavity structures.

Figure 2 shows the room-temperature photoluminescence from Ge quantum dots in a photonic crystal microcavity. Strong PL signal is observed in the range from 1.3 to 1.6μm. No signal is observed in a pattern-free region under the same conditions, which indicates that optical resonance in the cavity causes significantly enhancements. Multiple sharp peaks dominate the luminescence spectrum, while no obvious off-resonant luminescence is observed. The quality factors (Q) of these resonant peaks are in the range of 300–600. The wavelength of the resonant peaks can be adjusted by tuning the lattice constant of the photonic crystal structure.

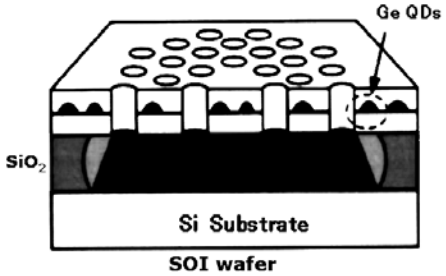

Fig. 1 Schematic structure of a photonic crystal microcavity with Ge self-assembled quantum dots on slicon-on-insulator (SOI) wafer.

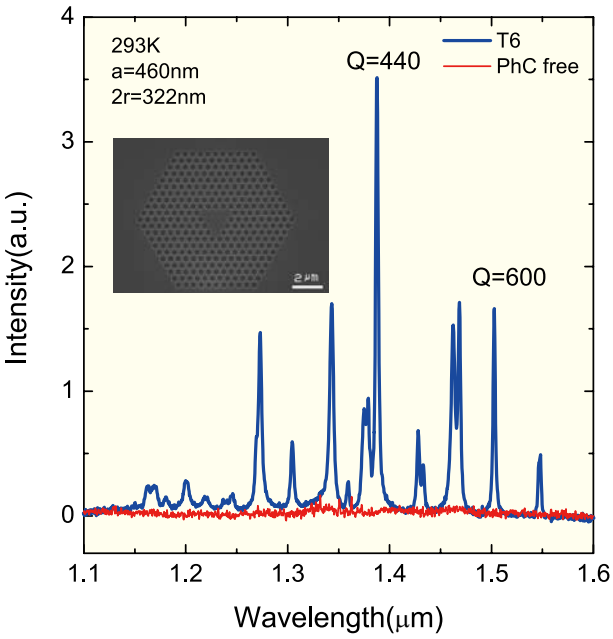

Fig. 2 RT PL signal from a T6 photonic crystal microcavity. The inset shows the SEM picture of the device.

As a step towards practicable devices, recently, a current-injected light emitting device was fabricated through embedding Ge dots into a Si microdisk with a p-i-n junction for current-injection. Resonant electroluminescence spectrum was recorded at room-temperature [3].

Silicon-based light-emitting devices are highly desired for the hybrid optoelectronic integration on Si to make it more powerful. Embedding self-assembled Ge quantum dots into optical microcavities is a promising direction, which is fully compatible with CMOS technology.

References

[1] J. Xia, R. Tominaga, S. Fukamizu, N. Usami, and Y. Shiraki, Japanese Journal of Applied Physics, 48, 022102 (2009).

[2] J. S. Xia, R. Tominaga, N. Usami, S. Iwamoto, Y. Ikegami, K. Nemoto, Y. Arakawa, Y. Shiraki, Journal of Crystal Growth, 311, 883 (2009).

[3] J. Xia, Y. Takeda, N. Usami, T. Maruizumi, and Y. Shiraki, Opt. Express, 18, 13945(2010).

Key Words

Si-based Light-emitting Device, Ge Self-assembled Quantum Dots, Microcavity

Contact to

Jinsong Xia (Advanced Research Laboratories, Tokyo City University)
E-mail: jinsongxia@gamil.com

Noritaka Usami (Crystal Physics Division, IMR, Tohoku University)
E-mail: usa@imr.tohoku.ac.jp

Static Heterogeneity with a Certain Correlation Length in Metallic Glasses

We have investigated acoustic-phonon behavior of Pd-, Pt-, and Zr-based metallic glasses with the combination of inelastic x-ray scattering (IXS) and ultrasonic (US) measurements. The measured acoustic phonon behavior can be qualitatively explained by the elastic-wave scattering theory with a structural heterogeneous model.

Disordered materials, liquids and glasses, exhibit complex relaxation processes. The correlation between these dynamic processes and glass structure is one of main issues in glass science. Recently, we reported deterioration of the structure of a glass near the glass transition temperature due to the combined action of external megahertz frequency vibrations and β relaxation. The partially crystallized microstructure of a Pd-based metallic glass under sub-megahertz vibration strongly indicates that the atomic motions associated with the Johari-Goldstein β relaxation are spatially localized. Based on our experimental results on a transmission electron micrograph, we proposed a microstructural model of metallic glasses that consists of strongly-bonded regions surrounded by weakly-bonded regions [1]. To confirm the validity of the model, here we have investigated systematically the acoustic properties of some Pd-, Pt-, and Zr-based metallic glasses by the combination of inelastic x-ray scattering (IXS) and ultrasonic (US) measurements with the aid of the elastic wave scattering theory. In the cases of PdNiCuP, PdCuP, and PtNiP, the sound velocity of the phonons at low Q exceeds the US velocity, whereas the former goes close to the latter in the cases of ZrAlNiP, ZrAlNiCu and ZrCuAl, as seen in Fig. 1. Moreover, the wavelength (λ)-dependence of $L \sim \Omega_Q/Q\Gamma_Q$ representing the mean free path of phonon was also evaluated for the six metallic glasses. The L values of all the glasses tend to increase with increase in λ and steeply change at a certain value of λ (λ_c). It is found that the λ_c values for PdNiCuP, PdCuP, and PtNiP glasses are larger than those for Zr-based metallic glasses. In the light of the elastic wave scattering theory with the present structural heterogeneous model, it is strongly supported that the elastic inhomogeneity with a certain correlation length exists even in dense metallic glasses, as seen in Fig. 2. The present results indicate that Zr-based metallic glasses are more homogeneous than the Pt- and Pd-based metallic glasses [2].

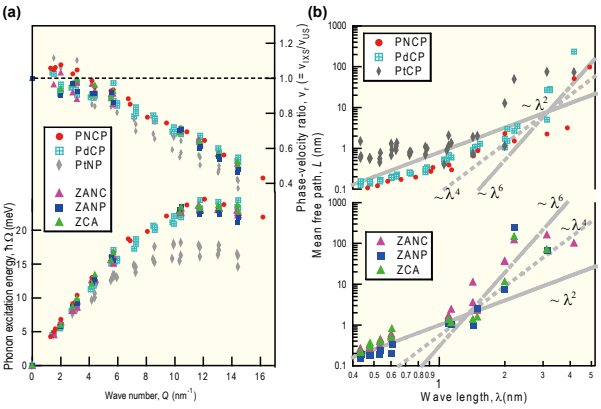

Fig. 1 (a) The phonon dispersion relation (lower panel) and relative phase velocity to ultrasound (upper panel) of six types of metallic glasses, which were obtained from the IXS spectra. (b) The wavelength (λ)-dependence of the mean free path L of acoustic phonon obtained for six glasses.

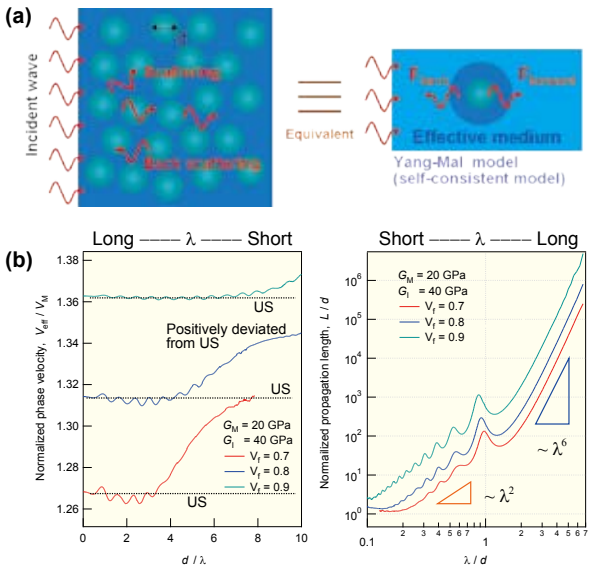

Fig. 2 (a) Schematic figure illustrating the two-dimensional heterostructure model of glass, consisting of hard inclusions embedded in a softer matrix. (b) The effective phase velocity relative to that in the matrix as a function of the inverse of wavelength and the propagation length as a function of wavelength for a composite material calculated with the effective medium self-consistent theory. The volume fraction of inclusion is set at V_f = 0.7, 0.8, and 0.9. The effective phase velocity is normalized the phase velocity of the matrix V_M. G_I = 40 GPa and G_M = 20 GPa.

References

[1] T. Ichitsubo *et al.*, Phys. Rev. Lett. **95**, 245501 (2005).
[2] T. Ichitsubo *et al.*, Phys. Rev. B **81**, 172201 (2010).

Key Words

Metallic Glass, Structural Heterogeneity, Phonon Dispersion

Contact to

Tetsu Ichitsubo (Department of Materials Science and Engineering, Kyoto University)
E-mail: tichi@mtl.kyoto-u.ac.jp
URL: http://www.mdsgn.mtl.kyoto-u.ac.jp/htms/members/ichitsubo/index.htm

Neutron Irradiation Effect on Superconducting Magnet Materials

New large scale fusion devices require a data base on neutron irradiation effect of fusion magnet, because the devices will generate high energy neutrons. To investigate mechanisms of irradiation effect and pile up the data base, neutron irradiation tests were conducted and post irradiated tests were performed.

Superconducting strands including NbTi, Nb_3Sn and Nb_3Al were prepared for neutron irradiation [1, 2]. The strands were irradiated by 14 NeV neutron at Fusion Neutronics Source in JAEA and the post irradiated tests were carried out at High Field Laboratory for Superconducting Materials in Tohoku University.

The results of the critical current measurements after irradiation are shown in Fig. 1. The Nb_3Sn strand showed that the critical current in the lower field increased remarkably as an increment of the neutron fluence. The border magnetic field (arrows in Fig. 1) where the critical current starts to get away from the non-irradiated critical current curve shifts to the higher magnetic field when the fluence increases. So, the increment of the critical current becomes larger in the lower field. The results of the critical field measurements under 100 mA showed no clear changes. However, the critical temperature measurements presented that the critical temperature after irradiation to 3.10 x 10^{21} n/m^2 decreased about 0.2 K.

The fast neutron knocks on the atoms in the matrix and makes interstitials and vacancies. When the damage increases with the higher neutron fluence, the field flux pinning force would be strengthened and the critical current would increase in the higher field. At the same time, the A-15 crystal structure would be disordered and the critical temperature decreased.

Regarding the electric insulation materials, epoxy resin blended with cyanate ester was used for trial GFRP fabrication. It has 10 polyimide film layers and 11 glass cloth layers. The vacuum impregnation process was adopted and

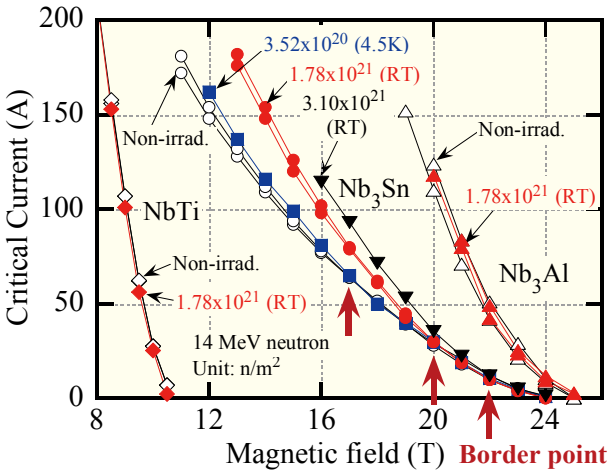

Fig. 1 Change in critical current against magnetic field after 14 MeV neutron irradiation.

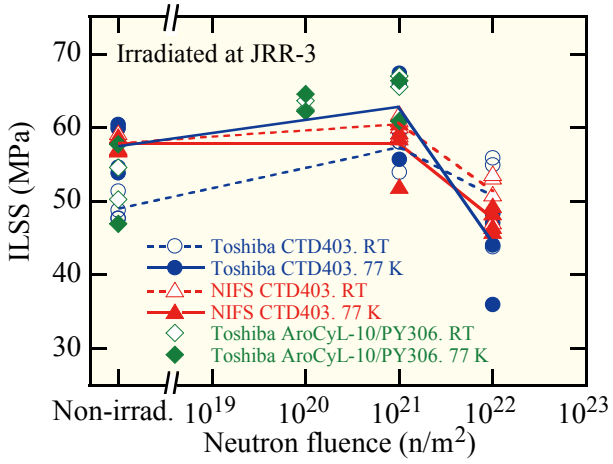

Fig. 2 Change in ILSS against neutron fluence. CTD403 shows 100 % cyanate ester resin. AroCyL-10/PY306 is blended resin with cyanate ester/epoxy of 40/60 in weight.

it was cured at 150 degree C. After machining the specimen for short beam test (10 mm^W x 15 mm^L x 2.5 mm^t), the specimens were irradiated by fission neutron at JRR-3 in JAEA and the short beam tests were carried out at RT and 77 K at Oarai center.

The results are shown in Fig. 2 [3]. Depending on the fabricated plate, the interlaminar shear strength (ILSS) becomes different but the scatter of each data set is rather small and over 40 MPa of ILSS is obtained even after irradiation to 1.0 x 10^{22} n/m^2. The RT samples showed the bending fracture at the tension side but the 77 K samples showed the interlaminar fracture at the mid section of the plate thickness.

References

[1] A. Nishimura, T. Takeuchi, S. Nishijima, G. Nishijima, T. Shikama, K. Ochiai, N. Koizumi, Fusion Engineering and Design, **84**, 1425–1428 (2009).

[2] A. Nishimura, T. Takeuchi, S. Nishijima, K. Ochiai, G. Nishijima, K. Watanabe, and T. Shikama, Advances in Cryogenic Engineering, **56**, 255-262 (2010).

[3] A. Nishimura, Y. Izumi, S. Nishijima, T. Hemmi, N. Koizumi, T. Takeuchi, and T. Shikama, Advances in Cryogenic Engineering, **56**, 127-134 (2010).

Key Words

Fusion Magnet, Neutron Irradiation, Nb_3Sn

Contact to

Arata Nishimura (Department of Helical Plasma Research, National Institute for Fusion Science)

E-mail: nishi-a@nifs.ac.jp

Plutonium Migration in Compacted Bentonite Under Reducing Conditions by Electromigration Method

The electromigration method was applied to study the migration behavior of plutonium in compacted bentonite under reducing condition [1]. Plutonium migrated as a chemical form with positive charge through bentonite. Strong reducing condition changes the chemical form of plutonium, and accelerates the migration of plutonium in compacted bentonite.

For high-level radioactive waste disposal, corrosion products of carbon steel overpack diffuse into buffer materials and then maintain the reducing environment in the vicinity of the repository. This reducing condition is expected to retard the migration of redox-sensitive radionuclides. However, a rare study on plutonium diffusion in compacted bentonite is available, especially under reducing conditions. Therefore our research group have developed and carried out electro-migration experiments with source of iron ions supplied by anode corrosion of iron coupon in compacted bentonite.

A carbon steel coupon was assembled with bentonite saturated by contacting with water including 0.01M of NaCl into an apparatus for electromigration as shown in Fig. 1. A few micro liter of tracer solution containing 1kBq (7×10^{-12}mol) of ^{238}Pu was spiked on the interface between carbon steel coupon and bentonite before assembling. There was a reference electrode of Ag/AgCl and a counter electrode of platinum foil in the upper part of the apparatus with 0.01 M of NaCl solution. The carbon steel coupon was connected to a potentiostat as a work electrode and was supplied electrical potential in the range of -500 to 300 mV vs. Ag/AgCl electrode at 25°C for up to 168 h. After supplying electrical potential, the bentonite specimen was pushed out from the column and was sliced in steps of 0.3 to 2mm. Each slice was submerged in 1N HCl solution to extract plutonium and iron, and the liquid phase was separated by the centrifugal method. Then the supernatant was taken to be measured with alpha liquid scintillation counter for plutonium and with atomic absorption spectrometry for iron.

The concentration profiles of plutonium infiltrated in bentonite specimens at different potentials are shown in Fig. 2. Plutonium migrated from anode toward cathode as far as 1mm from the interface, and the penetration length of plutonium grew deeper as the higher potential supplied. This result indicated plutonium migrated as a chemical form with positive charge through bentonite. It has been reported that no movement could be measured for plutonium diffusion in a concrete-bentonite system under an oxidizing condition in an experimental period as long as 5 years [2]. Our results show much faster migration of plutonium than those reported. We assume the formation of diffusive trivalent plutonium converted from non-diffusive tetravalent by ferrous ions introduced into bentonite because the total amount of plutonium penetrated was increased depending on the amount of ferrous ions introduced into bentonite.

$$Pu^{4+} + Fe^{2+} \leftrightarrow Pu^{3+} + Fe^{3+} \quad (1)$$

The movement of ions under the influence of the electric potential gradient, hence electromigration, can be described with the dispersion-convection equation,

$$\frac{\partial C}{\partial t} = D_a \frac{\partial^2 C}{\partial x^2} - V_a \frac{\partial C}{\partial x} \quad (2)$$

where D_a is an apparent dispersion coefficient, V_a is an apparent migration velocity including mostly electromigration of iron and

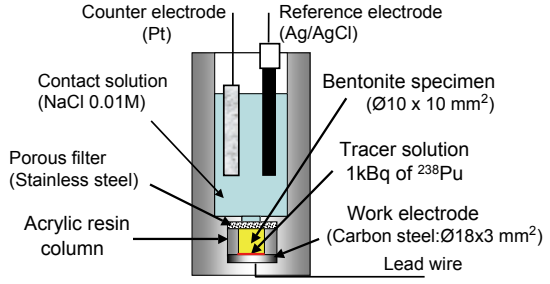

Fig. 1 Experimental apparatus for electromigration.

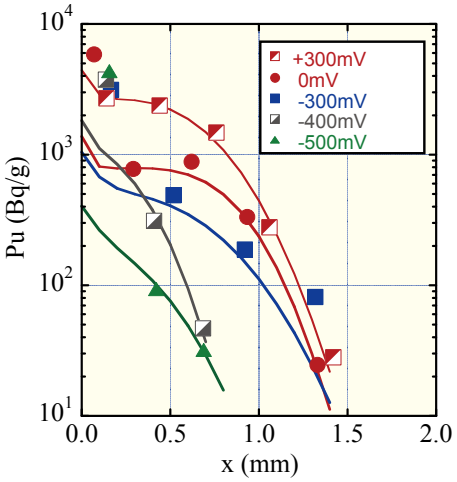

Fig. 2 Plutonium profiles in compacted bentonites by electromigration up to 168 h.

negligible electro-osmotic flow of water. To solve Eq.(2) with the boundary conditions in this experimental configuration, we considered successive spikes of ion in each time step, *M(t),* which is a function of the current. We obtained approximate solution as follows,

$$C(x,t) = \int_0^t \frac{M(t-\tau)}{2\sqrt{\pi D_a \tau}} \left[\exp\left\{ -\frac{(x-V_a\tau)^2}{4D_a\tau} \right\} + \exp\left\{ -\frac{(x+V_a\tau)^2}{4D_a\tau} \right\} \right] d\tau \quad (3)$$

Fitted curves are also plotted in Fig.2 for plutonium. We carried out the same analysis for iron.

Apparent diffusion coefficient of plutonium in bentonite can be calculated by the Einstein's relation.

$$D = \frac{uRT}{ZF} \quad (4)$$

where T is the temperature, Z is the valence of diffusing cation, and F is the Faraday constant, C. The mobility, u, could be obtained from following relation,

$$V_a = uE \quad (5)$$

where *E* is an electrical gradient in bentonite specimen. However, the electrical gradient in bentonite cannot be measured directly. So we tried to estimate the apparent diffusion coefficient of plutonium by comparing the migration velocity with iron ions. Applying Eq.(4) and Eq.(5) for both ions, following relation is obtained.

$$\frac{D_{Pu}}{D_{Fe}} = \frac{V_{a,Pu}}{V_{a,Fe}} \cdot \frac{Z_{Fe}}{Z_{Pu}} \quad (6)$$

The apparent diffusion coefficient of plutonium was estimated as not larger than 10^{-13} m^2/s by the comparison of migration velocity of plutonium and iron.

References

[1] K. Idemitsu, H. Ikeuchi, S. A. Nessa, Y. Inagaki, T. Arima, S. Yamazaki, T. Mitsugashira, M. Hara, Y. Suzuki , Proc. Materials Research Society Symposium on Scientific Basis for Nuclear Waste Management XXXII, Vol.1124, 283 (2009).

[2] Y. Albinsson, K. Andersson, S. Börjesson, B. Allard, J. Contaminant Hydrology 12, 189 (1996).

Key Words

Plutonium, Electromigration, Bentonite

Contact to

Kazuya Idemitsu (Department of Applied Quantum Physics and Nuclear Engineering, Kyushu University)

E-mail: idemitsu@nucl.kyushu-u.ac.jp

Development of Novel High Temperature Thermoelectric Materials

Doping of zinc to borosilicide was discovered to significantly improve the crystal quality even although zinc does not remain in the final product, and the thermoelectric power factor was increased by more than 30%. Zinc doping may lead to a way to improve the crystal quality of not just such borides and silicides but other compounds also

Boron is an interesting element, tending to form atomic network structures such as clusters and 2D atomic nets in compounds. This tendency is similar to carbon, which has been much more extensively studied for such materials as fullerenes, nanotubes, graphite-related materials, aromatics, etc. The rich materials science potential of boron remains to be tapped. Boron has one less electron than carbon and thus forms electron deficient atomic networks. However, this causes it to have a special affinity with the rare earth atoms, which are localized and fit in the voids of the atomic networks while supplying electrons. Numerous new rare earth boride compounds have been discovered in the past decade [1]. This is a good combination, because the rare earth atoms supply electrons to the robust boron atomic framework to stabilize and form novel structures, while at the same time the shell of f electrons will supply interesting properties like magnetism and can also enable tuning of the electrical properties (Fig. 1) [1].

One promising application is the use of boron cluster compounds as high temperature thermoelectric materials since they are quite stable materials and possess intrinsic low thermal conductivity [2]. Compounds such as p-type $RB_{44}Si_2$ and the series of $RB_{15.5}CN$, $RB_{22}C_2N$ and $RB_{28.5}C_4$ which exhibit intrinsic n-type behavior and may be the long awaited counterpart to boron carbide, are attracting particular interest [2]. The $RB_{44}Si_2$ compounds exhibit Seebeck coefficients in excess of 200 μV/K at high temperatures above 1000 K and also possess a low thermal conductivity of ~0.02 W/cm/K. We carried out a series of transition metal doping in an attempt to improve the properties. Zinc doping was found to have a striking effect, with the thermoelectric power factor increasing by more than 30% [3]. Surprisingly, analysis revealed that zinc is actually not retained in the

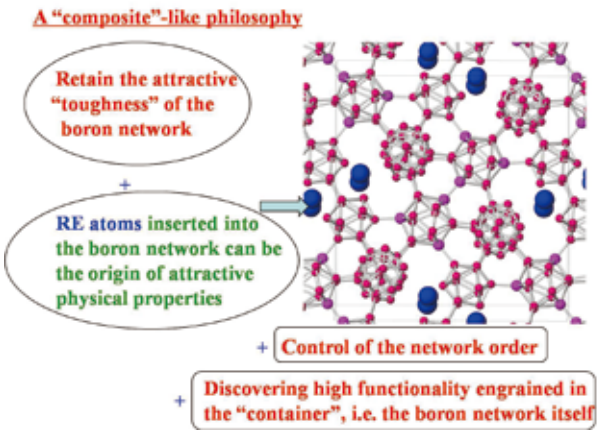

Fig. 1 Development strategy of boron network materials.

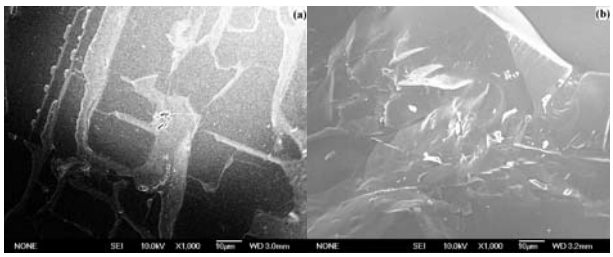

Fig. 2 SEM pictures of (a) undoped and (b) Zn doped $YB_{44}Si_2$.

sample. However, the addition of zinc to the synthesis is indicated to have an effect to significantly improve the crystallinity of the sample (Fig. 2(b)). Crystal quality had been a longstanding problem for the borosilicides, with imperfections in the form of Si aggregate regions existing (Fig. 2(a)).

This discovery of the zinc effect is exciting, since it may offer a simple way to improve crystal quality of not just borides or silicides but other high temperature compounds also.

References

[1] T. Mori, in Handbook on the Physics and Chemistry of Rare Earths, Vol. 38, ed. K. A. Gschneidner Jr., J. -C. Bunzli, and V. Pecharsky (North-Holland, Amsterdam, 2008) pp. 105-173.

[2] T. Mori and T. Nishimura, J. Solid State Chem., **179**, 2908-2915 (2006), T. Mori, Material Matters **4**, 37-39 (2009).

[3] T. Mori, D. Berthebaud, T. Nishimura, A. Nomura, T. Shishido, and K. Nakajima, Dalton Transactions **39**, 1027-1030 (2010). (Hot Article).

Key Words

Boron, Thermoelectric, Crystal Quality

Contact to

Takao Mori (Materials Nanoarchitectonics Center (MANA), National Institute for Materials Science (NIMS))
E-mail: MORI.Takao@nims.go.jp
URL: http://www.nistep.go.jp/achiev/ftx/jpn/stfc/stt103j/0910_03_featurearticles/0910fa02/200910_fa02.html

Toetsu Shishido (Advanced Research Center of Metallic Glasses, IMR, Tohoku University)
E-mail: shishido@imr.tohoku.ac.jp
URL: http://www.arcmg.imr.tohoku.ac.jp/topics/shishido.html

Metallic Glass Nanowires: Formation and Characterization

Metallic glasses (MG) are a promising class of materials that could find potential use as structural components in applications ranging from mobile phone casings to biomedical implants. At the same time, the realisation of MG structures on the nanoscale for novel applications has remained a challenge. We have developed a new method that is capable of producing MG nanowires showing that outstanding mechanical properties can be inherited into nanowire [1].

MGs are amorphous materials like window silica glass, but they are made from alloy metals. Although MGs visually look similar to crystalline metals like a steel, their amorphous structure leads to many advantages. For example, imperfections such as vacancy, dislocation, twin, and grain boundary in the crystalline metals are the main cause of mechanical failure. Owing to the amorphous structure, MGs possess a combination of unique properties including ultrahigh strength, high hardness, and high resistance to wear corrosion. For the practical engineering applications of such advantageous mechanical properties, there have been remarkable progresses in exploring alloy compositions that are best suited for the fabrication of bulk MGs [2]. However, far less attention has been paid to MG nanostructures, such as a wire.

We showed the self-organized amorphous nanowires that are formed on the fracture surfaces after conventional compression tests of bulk metallic glasses [3]. However, it was difficult to control their morphologies because they were created by instantaneous fracture processes. Recently, we have developed a mechanism to draw MG ribbons in a much more controlled fashion [1]. Our process follows a simple principle that glass blowers have been using for centuries. The MG is processed when it is still in a viscous liquid state under a tension that caused by a weight attached to the ribbon end drawn out into nanowires (Fig. 1).

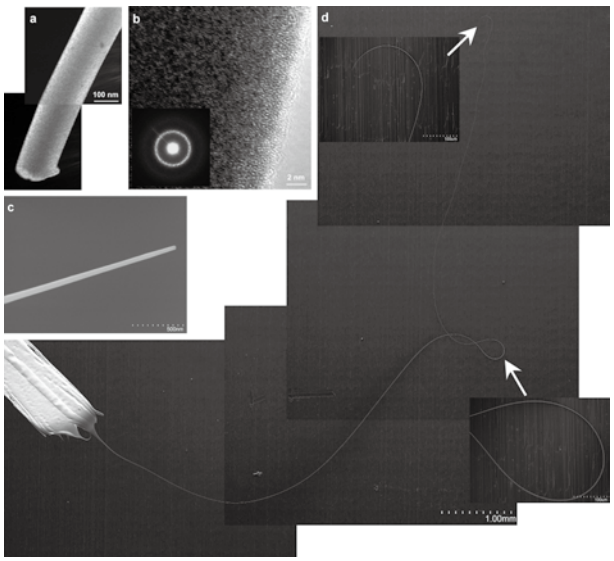

Fig. 1 A fast drawing of metallic glass ribbons above the grass transition temperature produces amorphous nanowires [1]. (a) TEM image of Zr based MG nanowire. (b) High resolution TEM and diffraction pattern reveal the amorphous states. (c) SEM image of Pd based MG nanowire having 40 nm in diameter. (d) The longest one has a total length of 1.3 cm.

We used a scanning laser Dopper vibrometer to measure the resonant frequences that deduces the Young's modulus beased on the Euler-Bernoulli beam theory. The modulus of the nanowires with the diameter range 250-1100 nm are much lower than that of the bulk counterpart owing to the hyper-excess free volume in nanowire and is tunable by heating.

The versatility of the drawing process ensures that MGs of a broad range of compositions can be formed in nanowire. In terms of future applications that depend on the composition elements used, Pd-based MG nanowires could be used as a highly sensitive hydrogen sensor. Fe-based MG nanowires exhibit soft magnetic properties that could be used for an ultrahigh magnetic-field sensor. These tough nanowires could be used in a large number of applications in nanotechnology.

References

[1] K. S. Nakayama, Y. Yokoyama, T. Ono, M. W. Chen, K. Akiyama, T. Sakurai, and A. Inoue, Adv. Mater. **22**, 372 (2010).

[2] A. Inoue, *Acta. Mater.* **48**, 279 (2000).

[3] K. S. Nakayama, Y. Yokoyama, G. Xie, Q. S. Zhang, M. W. Chen, T. Sakurai, and A. Inoue, Nano. Lett. **8**, 516 (2008).

Key Words

Nanowire, Metallic Glass, Young's Modulus

Contact to

Koji Nakayama (WPI-AIMR, Tohoku University)

E-mail: kojisn@wpi-aimr.tohoku.ac.jp

URL: http://www.wpi-aimr.tohoku.ac.jp/jp/index.php

Yoshihiko Yokoyama (Advanced Research Center of Metallic Glasses, IMR, Tohoku University)

E-mail: yy@imr.tohoku.ac.jp

URL: http://www.arcmg.imr.tohoku.ac.jp

Electrical Spin Injection in $L1_0$-FePt / GaAs based Ferromagnet Semiconductor Hybrid Structures

In the field of semiconductor spintronics, electrical spin injection, manipulation and detection are fundamental technologies for utilizing spin degree of freedom in semiconductors. Recently, perpendicularly magnetized thin film is paid much attention not only for the magnetoresistive random access memory (MRAM) but also as the spin injector source to semiconductors. We realize the high remanent magnetization of perpendicularly magnetized $L1_0$-FePt on a MgO / GaAs structure and apply to the electrical spin injection from $L1_0$-FePt to GaAs / AlGaAs light emitting diode (LED) through a MgO tunnel barrier.

Ferromagnetic metal (FM) / semiconductor (SC) hybrid structure is attracting much attention for realizing electrical spin injection and spin detection. In addition, since an effective magnetic field due to spin orbit interaction (SOI) is electrically controlled in semiconductor two dimensional electron gas (2DEG) [1], FM / SC hybrid structure is one of the promising candidates for realizing novel electronic devices based on spins. Since the SOI induced effective magnetic field is along an in-plane direction to the 2DEG, perpendicular spin injection becomes prerequisite for an electrical control of spin rotation. However, magnetic easy axis of conventional ferromagnetic film is the in-plane direction resulting in the application of an external magnetic field. $L1_0$-ordered FePt shows a large perpendicular magnetic anisotropy and a moderately high saturation magnetization. In addition, since the $L1_0$-FePt can be grown on a MgO layer which is used as a tunnel barrier for an efficient spin injection, $L1_0$-FePt is of considerable interest for spintronics materials [2].

We investigated the magnetic properties of $L1_0$-FePt on MgO / (001) *n*-GaAs structure for the high remanent magnetization and applied to the electrical spin injection from $L1_0$-FePt to GaAs / AlGaAs LED structure [3]. Perpendicularly magnetized FePt films were prepared at a substrate temperature T_s = 300 °C by magnetron sputtering and we measured the magnetic field dependence of polar magneto-optical Kerr signal in 5nm $L1_0$-FePt / 3nm MgO / GaAs. By post annealing at T_s = 350 °C for 60 min, the ratio of remanet magnetization to saturation magnetization drastically increases from 0.22 to 0.93, and the magnetization curve shows good squareness in the annealed film resulting in the perpendicularly magnetized FePt at a zero magnetic field. Then, we tried the electrical spin injection from $L1_0$-FePt to GaAs / AlGaAs LED. Figure 1 shows the magnetic field dependence of circular polarization in an electroluminescence (EL) and a photoluminescence (PL) at T = 10K. EL polarization shows the hysteresis loop with good squareness reflecting $L1_0$-FePt magnetic property. The hysteresis of PL polarization is originated from the magnetic circular dichroism, where the linear polarized light transmitting through the magnetic thin film changes to circularly polarized light due to the spin dependent density of state in magnetic materials. As a result, circular polarization due to the electrical spin injection becomes ±1% at B = 0T.

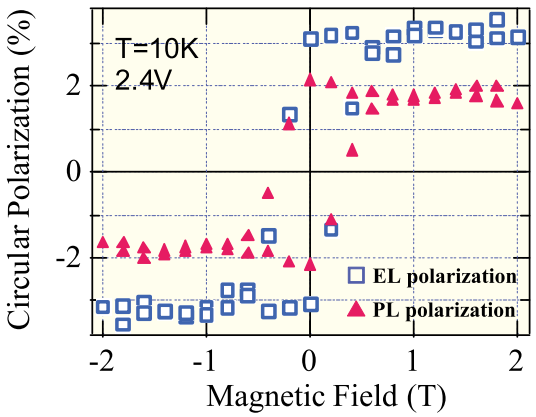

Fig. 1 Magnetic field dependence of circular polarization in $L1_0$-FePt / MgO / GaAs LED structure. Square and triangle plots show the results of EL and PL measurements, respectively.

Recently, MRAM based on current induced magnetization reversal is promising for the next memory generation. Perpendicularly magnetized magnetic tunnel junction based on $L1_0$-ordered ferromagnetic thin film is one of the candidates for realizing a small critical reversal current density and a high thermal stability. These MRAM technology combined with transistor structures, i.e. spin-MOSFET, will produce reconfigurable logic and logic-in-memory architecture for low energy consumption. Although the spin injection efficiency is still low due to the roughness at MgO / GaAs interface, the perpendicular spin injection into semiconductor will bring advances for future spintronics integrated systems.

References

[1] J. Nitta, T. Akazaki, H. Takayanagi, and T. Enoki, Phys. Rev. Lett. **78**, 1335 (1997).

[2] M. Kohda, A. Ohtsu, T. Seki, A. Fujita, J. Nitta, S. Mitani, and K. Takanashi, Jpn. J. Appl. Phys. **47**, 3269 (2008).

[3] M. Kohda, *et al*., in preparation.

Key Words

Spintronics, $L1_0$-FePt, Electrical Spin Injection

Contact to

Makoto Kohda (Department of Materials Science, Tohoku University)

E-mail: makoto@material.tohoku.ac.jp

URL: http://www.material.tohoku.ac.jp/~kotaib/top_e.html

Improvement of Critical Current Properties in MgB_2/Fe Tape Conductors

The critical current density of MgB_2 can be greatly improved through carbohydrate doping. This organic material can decompose at relatively low temperature, and generate reactive carbon atoms before the MgB_2 phase formation. The C can be incorporated into the MgB_2 crystal lattice by replacing boron, and thus B_{c2} is significantly enhanced due to selective tuning of impurity scattering of the π and σ bands in the two-band MgB_2. Besides the efforts of increasing B_{c2} by carbon doping, the fine grain size and nano-size inclusions caused by doping would create many flux pinning centres improving the J_c-B property of MgB_2.

One promising application of MgB_2 superconductor is the magnetic resonance imaging (MRI) magnet that can work at ~20 K, a temperature range that can be readily reached by a cryogen-free cryocooler. For this reason, a huge amount of work has been carried out to improve the current carrying capability of MgB_2 wires/tapes, so that they can be used to construct MRI magnets.

However, the pristine MgB_2 always shows lower J_c values because of low upper critical field (B_{c2}) and poor flux pinning. In order to improve J_c-B properties, a number of experimental techniques, including chemical doping, irradiation, magnetic field annealing, and ball-milling methods, have been attempted. Compared to other methods employed, chemical doping with carbon-containing materials was thought as the convenient and effective way to enhance the J_c-B properties of MgB_2.

Figure 1 shows transport J_c versus magnetic field curves for the $C_9H_{11}NO$ doped samples sintered at different temperatures. Compared to those for the undoped samples, the in-field J_c properties of $C_9H_{11}NO$ doped tapes were much improved, indicating an enhanced flux pinning ability. 4% doped samples show higher J_c than the 2% doped ones at each corresponding temperature, indicating a high doping tolerance of $C_9H_{11}NO$ in MgB_2. The highest J_c values were obtained for the 4% doped samples annealed under 800°C. For example, at 4.2 K, 10 T, J_c reached 3.7×10^4 A/cm^2 [1]. This is the highest Jc value observed for carbohydrate doped MgB_2 tapes

The melting point of $C_9H_{11}NO$ is only about 70°C, meaning that the $C_9H_{11}NO$ would be in liquid state before chemical reaction happens, making a homogeneously

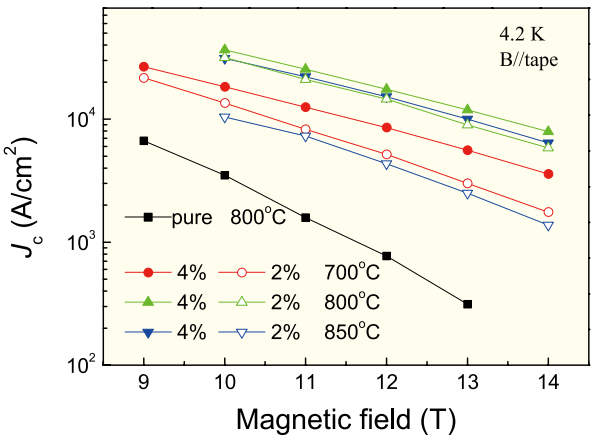

Fig. 1 Transport J_c-B properties of Fe-sheathed undoped and doped tapes.

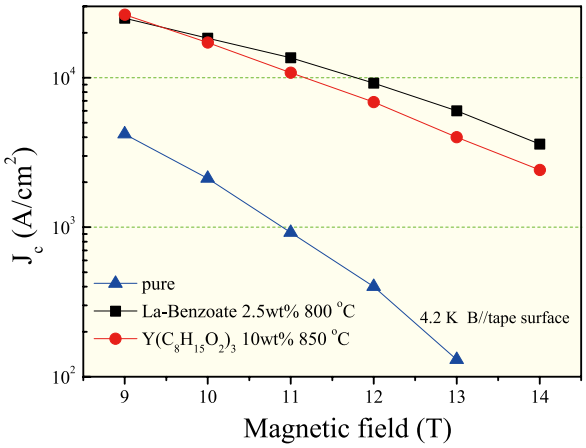

Fig. 2 J_c-B properties of pure and organic rare-earth salts doped tapes.

distribution in raw materials. On the other hand, $C_9H_{11}NO$ decomposes at a temperature below the formation temperature of MgB_2 phase, so it can provide highly reactive C during the formation of MgB_2 phase. The C element released from decomposition can effectively substitute into B sites. And the substitution of C for B induces disorder on the lattice sites, leading to the enhancement of the B_{c2}. This is thought as the main reason for the superior field dependence of J_c in the $C_9H_{11}NO$ doped tapes.

Recently, we also realized the simultaneous introduction of "scattering + pinning" using a single dopant of organic rare earth salt. Figure 2 presents the transport J_c at 4.2 K in magnetic fields for two organic rare earth salts doped samples. It is evident that both doped tapes exhibited superior J_c values, at 4.2 K and in a field of 12 T, the J_c value for La-Benzoate doped tape reached 1.84×10^4 A/cm^2, 23 times higher than that of undoped samples.

Therefore, the present addition acts as a codopant or reactive nano-carbon, combining a C substitution induced B_{c2} enhancement and stronger flux pinning induced by nanosize precipitates, thus leading to the excellent J_c-B performance of the doped tapes. The results suggest that organic material has to be considered as a promising dopant for enhancing the current capacity of MgB_2 conductors.

References

[1] X. P. Zhang, D. L. Wang, Z. S. Gao, L. Wang, Y. P. Qi, Z. Y. Zhang, Y. W. Ma, S. Awaji, G. Nishijima, K. Watanabe, E. Mossang, X. Chaud, Supercond. Sci. Technol. **23**, 025024 (2010).

Key words

MgB_2, Doping, Critical Current Density

Contact to

Yanwei Ma (Institute of Electrical Engineering, Chinese Academy of Sciences)

E-mail: ywma@mail.iee.ac.cn

Kazuo Watanabe (High Field Laboratory for Superconducting Materials)

E-mail: kwata@imr.tohoku.ac.jp

Magnon Localization in Quantum Spin System NH_4CuCl_3

How the ground state of field-induced magnons in quantum spin systems is determined? Two isomorphic quantum spin systems $TlCuCl_3$ and NH_4CuCl_3 show the quite different ground state. The former enjoys the realization of Bose-Einstein Condensation at low temperatures as well known, while the latter shows the magnetization plateaus indicating the crystallization of magnons. We have microscopically investigated the ground state of NH_4CuCl_3 under high magnetic fields and found that magnons localize at low temperatures to form a crystal.

In last two decades, quantum spin systems have been attracting much interest both experimentally and theoretically because they exhibit numerous peculiar magnetic features such as a spin gap and a magnetization plateau, which cannot be interpreted by conventional classical spin models. When a magnetic field is applied in a spin gap system, the energy of the one of the triplet states is lowered due to the Zeeman interaction so that the spin gap vanishes at the critical field. Then the ground state becomes magnetic so that the magnetic ordering occurs if there are three-dimensional interactions. Such field-induced magnetic ordering has been observed in the spin gap systems $KCuCl_3$ and $TlCuCl_3$. The field-induced magnetic ordering was captured as the Bose-Einstein condensation of magnons by mapping the spin gap system to the system consisting of boson with magnetic moment. On the other hand, the title compound NH_4CuCl_3, which are isomorphous of the former two show the two-stepped magnetization plateaus at one-quarter and three-quarters of the saturation magnetization (Fig. 1), indicating the localization of the magnons, though their periodic structure is still controversial.

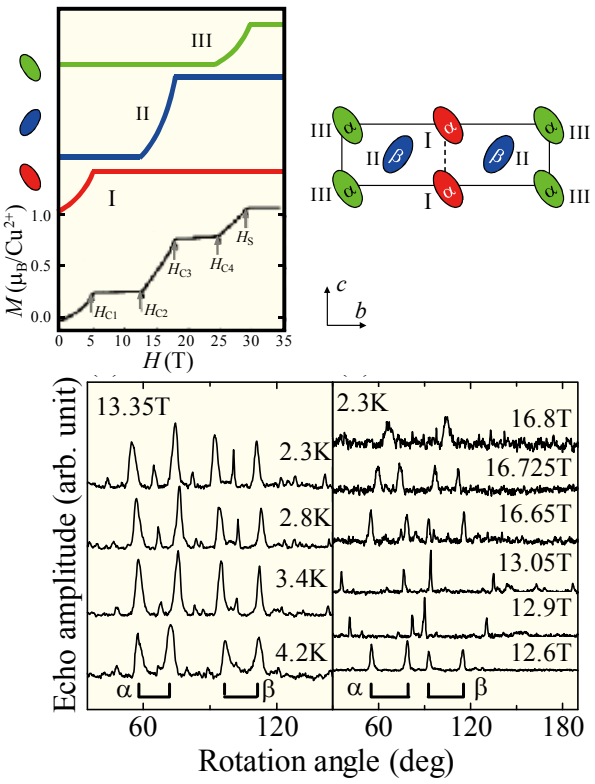

Fig. 1 Magnetization curve with the two-stepped plateaus, spatial allocation of dimers in NH_4CuCl_3, and Cu-NMR spectra under magnetic fields $H_{c2}<H<H_{c3}$.

We have carried out $^{63/65}$Cu-, $^{35/37}$Cl-NMR experiments under high magnetic field in order to investigate the triplet localization in NH_4CuCl_3. In the $^{63/65}$Cu-NMR experiments at the 1/4-plateau phase, the NMR spectra at the singlet Cu site were only observed because those at the triplet Cu site are wiped out due to the strong spin fluctuation of onsite 3d-spins. It was found that the temperature dependence of the shift of $^{63/65}$Cu-NMR spectra at the singlet Cu site deviates from that of macroscopic magnetization below T=6 K. This deviation reflects the triplet localization in this system, because the localized triplets contribute only to the macroscopic magnetization but to the Knight shift of the NMR-visible singlet site. The result of $^{35/37}$Cl-NMR also supports this idea.

We also performed the $^{63/65}$Cu-NMR experiments at high magnetic fields between the one-quarter and the three-quarters magnetization plateaus. There are two kinds of dimers referred as α, β with different orientation in crystal (Fig. 1). These two can be separately detected by NMR spectra. Theoretical models proposed so far tried to explain the plateaus in terms of the three inequivalent dimers (I, II, III) with different critical fields (0, H_{c2}, H_{c4}). In those models, it is expected that the signal amplitude of α and β differs in the field region $H_{c1}<H<H_{c3}$, where the dimer I is saturated and hence should be wiped out. However, our NMR results [1] articulately show that α and β dimers in singlet state have the same number density in the field region. This result imposes a strong limit onto theoretical models for the spatial allocation of the localized triplets.

References

[1] H. Inoue, S. Tani, S. Hosoya, K. Inokuchi, T. Fujiwara, T. Saito, T. Suzuki, A. Oosawa,T. Goto, M. Fujisawa, H. Tanaka, T. Sasaki, S. Awaji, K. Watanabe, N. Kobayashi, Phys. Rev. B**79**, 174418 (2009).

Key Words

Quantum Spin System, High-field NMR, Magnetization Plateau

Contact to

Takayuki Goto (Department of Physics, Faculty of Science and Technology, Sophia University)

E-mail: gotoo-t@sophia.ac.jp

URL: http://www.ph.sophia.ac.jp/~goto-ken

Takahiko Sasaki (Low Temperature Physics Division, IMR, Tohoku University)

E-mail: takahiko@imr.tohoku.ac.jp

Neutron Diffraction in 30 T Pulsed High Magnetic Fields

A non-trivial magnetic structure is often induced when interactions are competing for geometrical frustration. The neutron diffraction is the key experiment in such case. We have developed a neutron diffraction instrument under very strong magnetic field up to 30 Tesla based on the international collaboration project of ICC-IMR. It has been used at the world leading neutron facilities such as J-PARC, SNS and ILL.

Magnetic field is a powerful tuning parameter of magnetic properties of matters. It induces new states with non-trivial magnetic structures in geometrical frustrated antiferromagnets. When interactions are competing each other for the special arrangement/network of magnetic moments, it is impossible to satisfy all interactions. In this case, the ground state energy is highly degenerated. When a magnetic field is applied, the degeneracy is partly lifted and some state falls into the lowest energy. A situation is more complicated when there is a finite spin-lattice coupling. In such case, there is another route to lift the degeneracy of the ground state. Namely, the geometrical frustration can be partly resolved by the lattice deformation. A series of Cr-spinel compounds XCr_2O_4 (X=Cd, Hg, Zn) belong to this class of material. It is known to show the spin Jahn-Teller effect.

In XCr_2O_4, a non-trivial half-magnetization plateau has been found in the ordered state [1]. Different from the conventional plateau stabilized by magnetic anisotropy, it appears irrespective of magnetic field direction. To understand the origin of this anomalous behaviour, it is necessary to determine the magnetic structure at the plateau state. For X=Hg, the task was completed by means of neutron diffraction in a steady magnetic field. For X=Cd, the plateau starts at 28 T, which is far beyond the steady magnetic field available for neutron diffraction.

Fig. 1 A portable capacitor bank of neutron diffraction, which is installed at JRR3 reactor. It can be set into a limited space of a spectrometer.

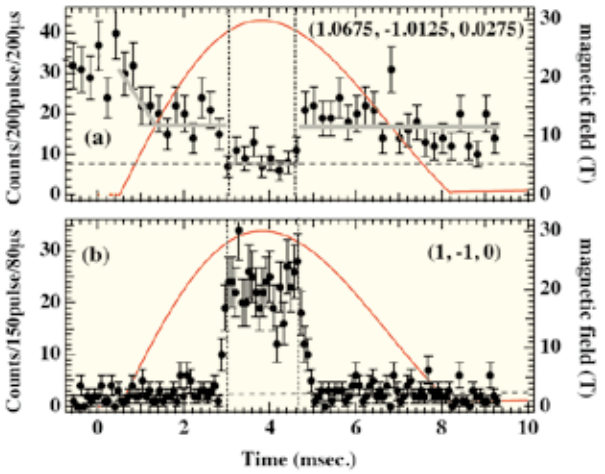

Fig. 2 Field dependence of bragg peak intensity at (a) incommensurate and (b) commensurate positions. The intensity alternates at 28 T. The commensurate-incommensurate transition is directly confirmed by the present neutron diffraction.

Recently, we have made a new breakthrough by developing a 30 Tesla portable miniature pulsed magnet for neutron diffraction. Because of the compact design of the magnet, we can use it without any modification of the spectrometer. Thanks to the very small magnet volume, a compact mobile capacitor bank can be used as a power supply as shown in Fig. 1.

Figure 2 shows the result of neutron diffraction up to 30 T [2]. The bragg peak moves from the incommensurate position to commensurate one above 28 T. It is the first direct determination of the magnetic structure at the half-plateau state. By measuring several different peaks, magnetic structure can be refined. The obtained structure is found to be common between Hg and Cd derivatives. It indicates that there is a universal mechanism of spin-lattice coupling in this series of materials.

The present result has established the pulsed high magnetic field neutron diffraction as a powerful new tool for investigating magnetic compounds. A technical transfer has been made to foreign institutes by the ICC-IMR collaboration scheme.

References

[1] H. Ueda *et al.*, Phys. Rev. Lett. **94**, 047202 (2005).
[2] M. Matsuda *et al.*, Phys. Rev. Lett. **104**, 047201 (2010).

Key Words

Neutron Diffraction, High Magnetic Field, Spin Jahn-Teller Effect

Contact to

Hiroyuki Nojiri (Magnetism Division)
E-mail: nojiri@imr.tohoku.ac.jp
URL: http://hfpm.imr.tohoku.ac.jp